Controlling the Electrical and Magnetoelectric Properties of Epitaxially Strained $Sr_{1-x}Ba_xMnO_3$ Thin Films

Eric Langenberg*, Laura Maurel, Noelia Marcano, Roger Guzmán, Pavel Štrichovanec, Thomas Prokscha, C. Magén, Pedro A. Algarabel, José A. Pardo

Dr. E. Langenberg, Dr. N. Marcano, Dr. P. Štrichovanec, Prof. P. A. Algarabel
Instituto de Ciencia de Materiales de Aragón (ICMA), Universidad de Zaragoza-CSIC, 50009 Zaragoza, Spain
E-mail: eric.langenberg.perez@gmail.com

Dr. E. Langenberg, Dr. L. Maurel, Dr. C. Magén, Prof. P. A. Algarabel
Departamento de Física de la Materia Condensada, Universidad de Zaragoza, 50009 Zaragoza, Spain

Dr. L. Maurel, Dr. R. Guzmán, Dr. C. Magén, Dr. J. A. Pardo
Instituto de Nanociencia de Aragón (INA), Universidad de Zaragoza, 50018 Zaragoza, Spain

Dr. R. Guzmán, Dr. C. Magén, Dr. J. A. Pardo
Laboratorio de Microscopías Avanzadas, Universidad de Zaragoza, 50018 Zaragoza, Spain

Dr. N. Marcano
Centro Universitario de la Defensa, Academia General Militar, 50090 Zaragoza, Spain

Dr. T. Prokscha
Laboratory for Muon Spin Spectroscopy, Paul Scherrer Institute-CH-5232 Villigen PSI, Switzerland

Dr. C. Magén
Fundación ARAID, 50018 Zaragoza, Spain

Dr. J. A. Pardo
Departamento de Ciencia y Tecnología de Materiales y Fluidos, Universidad de Zaragoza, 50018 Zaragoza, Spain

The perovskite (Sr,Ba)MnO_3 system is an ideal candidate for tailoring electrical and magnetoelectric properties through the accurate control of Ba-content and epitaxial strain due to the strong coupling between polar instability, spin order and lattice. Here, first, the polar order is proved to be induced in $Sr_{1-x}Ba_xMnO_3$ thin films through lattice expansion either by epitaxial strain or chemical pressure, which correlates with the evolution of the dielectric properties. Second, due to strong spin-phonon coupling, a large magnetoelectric response is found in the (Sr,Ba)MnO_3 system, in which the dielectric constant drops up to 50% when the antiferromagnetic order emerges, larger than most magnetoelectric oxides. More important, this coupling between magnetism and dielectric properties can be tuned from ~18% to ~50% by appropriately selecting Ba-content and epitaxial strain. Third, a clear tendency to increase the band gap energy on increasing the unit cell volume either by epitaxial strain or chemical pressure is found, which opens the way for engineering the semiconducting properties of (Sr,Ba)MnO_3 system at will. Thus, this work proves the possibility to design the electrical response and the magnetoelectric coupling in (Sr,Ba)MnO_3 system.

Keywords: magnetoelectrics, multiferroics, impedance spectroscopy, dielectrics, semiconductors

1. Introduction

Transition metal oxides, particularly those with the perovskite structure (ABO_3), exhibit a wide range of interactions due to the strongly polarizable metal-oxygen bond, the strong correlation of the *d* electrons, and the variable oxidation state of the transition metal cations.[1,2] As a result, a large variety of properties and cooperative phenomena may emerge such as metallic/semiconductor/insulating behavior, superconductivity, polar instability, ferroelectricity, different magnetic orders, thermoelectricity or high dielectric constant, among others.[1,2,3] More important, the energy scales of the different interactions are similar in magnitude, giving rise to strong couplings between spin, electron, orbital, and lattice/phonon degrees of freedom. Thus, multiple low energy phases –with different functionalities– are accessible by small perturbations such as epitaxial strain or chemical replacements, for instance.[1,4] These complex perovskite oxides provide an interesting playground to tune, design and engineer novel properties that go beyond present-day technologies.

Here we focus on (Sr,Ba)MnO_3 system. In these compounds, in the perovskite phase, a strong coupling between polar instability, spin order and lattice is expected.[5,6,7] The expansion of the lattice either by strain engineering or chemical pressure (by replacing Sr with Ba) favors the non-centrosymmetric distortion.[5,6,7] Bulk centrosymmetric $SrMnO_3$ (SMO) was found to be polar in 1.7% strained epitaxial thin films[8] and ferroelectric in bulk $Sr_{1-x}Ba_xMnO_3$ (SBMO) for $x > 0.4$.[9] The coupling between spin and lattice enables moderate epitaxial strains to severely modify the magnetic interactions, and eventually the magnetic ground states in SMO.[6,10] The magnetic order strongly couples with the polar instability since both are driven by the Mn cations,[5,6,7,9,11] thus giving rise to an expected strong magnetoelectric coupling.[12,13]

Recently, the perovskite phase in SBMO films was synthesized for the first time with Ba-contents in the range $0.2 \leq x \leq 0.5$ grown on different perovskite substrates.[14] Note that the hexagonal phase is far more stable than the perovskite phase, especially for large Ba-contents.[15,16] Using simultaneously epitaxial strain and Ba substitution yields large structural changes in SBMO,

in which much greater tetragonal distortions were achieved than in bulk specimens.[14] Due to the aforementioned couplings in (Sr,Ba)MnO_3 system, these large lattice distortions may have an important effect on the dielectric, semiconducting and magnetoelectric properties, which have not been explored so far.

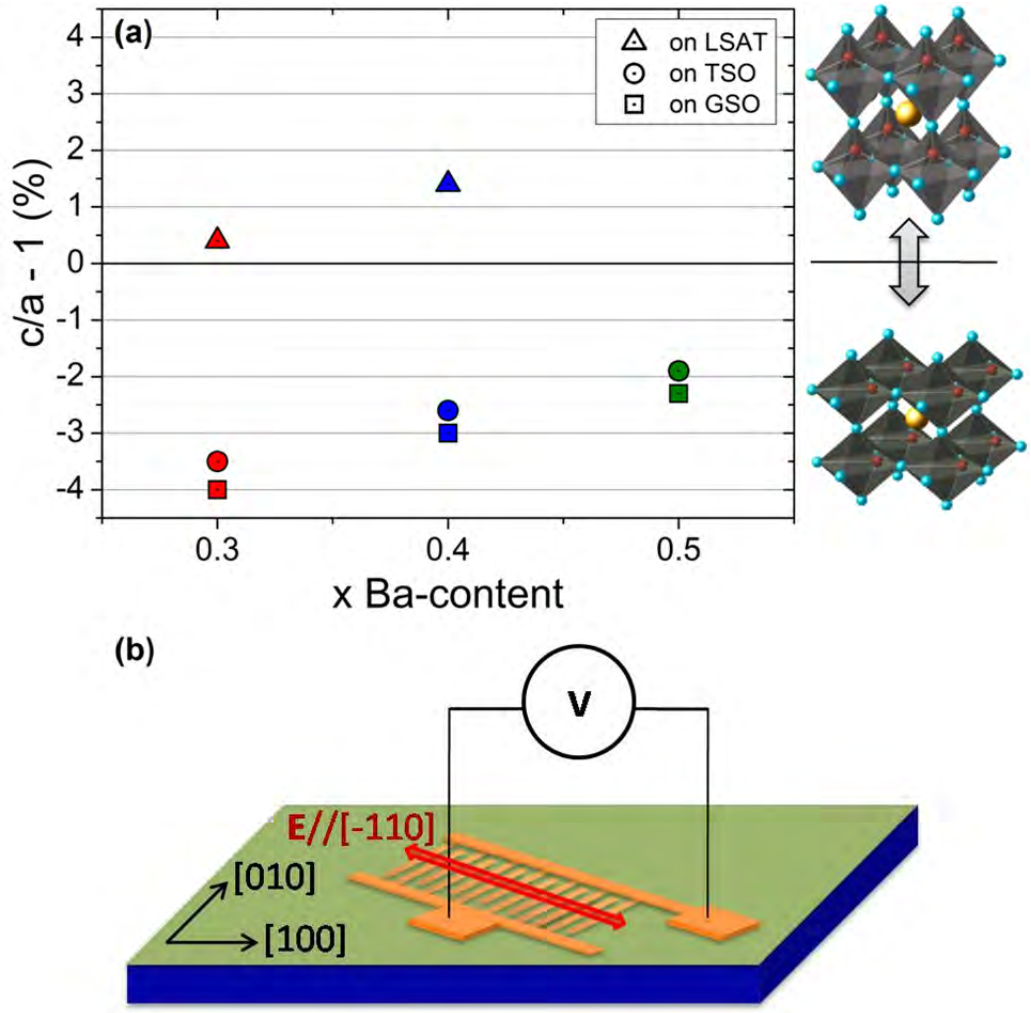

Figure 1. (a) Tetragonal distortion of the $Sr_{1-x}Ba_xMnO_3$ thin films analyzed in this work as a function of the Ba-content and substrate. **(b)** Sketch of the interdigital electrodes patterned for the electrical characterization of $Sr_{1-x}Ba_xMnO_3$ thin films.

The aim of this work is to set the basis for controlling these electrical and magnetoelectric properties by appropriately selecting the Ba-content and the epitaxial strain. For this purpose, we have selected three Ba-compositions: (x = 0.3, 0.4 and 0.5), grown on three different substrates: $(LaAlO_3)_{0.3}(Sr_2AlTaO_6)_{0.6}$ [LSAT], $TbScO_3$ (TSO) and $GdScO_3$ (GSO), as shown in **Figure 1**a, where the tetragonal distortion is expressed in terms of $t \equiv c/a-1$ (c and a denote the out-of-plane and in-plane lattice parameters, respectively), i.e. in terms of deviations from the cubic structure.

Thus, positive values correspond to an elongated out-of-plane lattice parameter with regard to the in-plane lattice parameter, whereas negative values refer to the opposite. Note that *a* and *c* lattice parameters of the strained SBMO films of this work were previously determined in Ref. [14].

In-plane impedance spectroscopy by means of interdigital electrodes (IDE's) –see Experimental section and Supporting Information– was used to determine the electrical properties of the SBMO thin films, as sketched in Figure 1b. Impedance spectroscopy is a powerful technique to analyze and disentangle all electrical contributions to the impedance of the system.[17,18,19,20,21,22,23] Moreover, it allows deconvoluting pure dielectric response from the electrical resistance of the sample.[17,18,19,20,21,22,23] Impedance spectroscopy in thin films is commonly performed along the out-of-plane direction through a parallel-plate capacitor configuration, i.e. by placing the film between bottom and top electrodes. Yet, for poorly insulating materials, especially for very thin films (our SBMO films are thinner than 20 nm, see Supporting Information), the very low resistance of the film hinders the measurement of the dielectric response in the parallel-plate capacitor configuration. SMO is predicted to possess a small semiconductor band gap (0.2 – 0.3 eV),[6, 24] so poorly insulating features may be expected for Ba-doped samples. Instead, in-plane electrical measurements are preferable as they lead to much larger measurable film resistance due to the longer separation between finger electrodes (microns instead of nm) and the small cross section arising from the low thickness.[25,26]

From our previous work,[8] the polar axis in tensile-strained (001)-oriented SMO thin films lies along the in-plane <110> directions. As SBMO samples analysed in this work (except for $Sr_{0.6}Ba_{0.4}MnO_3$ on LSAT) display c/a < 1 (Figure 1a), they are also tensile-strained and we expect that the polar axis, if present, may lie along the same <110> in-plane directions.[27] Thus, to maximize the possible changes in the dielectric response of strained SBMO films in the vicinity of the polar transition temperature, IDE's were deposited in such a manner that the electric field is applied along the [110] direction, as depicted in Figure 1b.

2. Results and discussion

2.1 Impedance data and model

Figure 2a-c shows examples of the complex impedance spectra ($Z^* = Z' + iZ''$) of SBMO films grown on LSAT (x = 0.3, 0.4) and GSO (x = 0.5) recorded at different temperatures. The common representation of plotting the negative imaginary term, $-Z''$, versus the real term, Z', of the complex impedance is used.[17] Note that the angular frequency, ω, of the applied signal [$V_{ac} = V_0\sin(\omega t)$, see Experimental section] is indirectly present in these impedance complex planes, as indicated in Figure 2a-c. The data signal the existence of one unique incomplete semicircle, the radius of which decreases upon increasing temperature. The same trend (not shown here) is found in the rest of SBMO films analyzed in this work in the whole temperature range (10 K – 400 K). These semicircles in $-Z''$ *vs.* Z' impedance complex planes are in full agreement with the characteristic impedance response of any dielectric material, modelled by a resistor, *R*, and capacitor, *C*, in parallel, accounting for the opposition to the flow of charge carriers and the ability of the dielectric to store charge, respectively.[17] The semicircle radius corresponds to $R/2$ and its decrease on increasing temperature indicates that the resistance of the sample decreases upon increasing temperature, as expected for semiconducting materials. It is worth remarking here that the impedance spectra recorded for LSAT, TSO and GSO bare substrates (see Supporting information) show much larger resistance than SBMO films on top of them and consequently the drop of the applied voltage mostly takes place in SBMO.

The fact that only one semicircle is found in the whole temperature range points to negligible extrinsic contributions in the system, if present at all. Note that extrinsic contributions evidenced by two or more semicircles are clearly present in other cases.[18,20,21,22,23,28,29] The absence of these common extrinsic contributions in our films possibly come from the large resistance on measuring through in-plane IDE's configuration. Still, careful analysis of impedance data at very high frequencies (above ≈ 10 MHz) signals a small inductance contribution (see Supporting information). Note that the impedance of an inductor, *L*, increases upon increasing frequency ($Z_L =$

iωL) and becomes non-negligible at very high frequencies. This inductive contribution comes from the inductance of the wires, L_0, which is impossible to rid completely, but has been diminished to the lowest possible value by appropriate experimental set up. Indeed, the recorded inductance values of the system are tiny and temperature-independent, as we will comment later on.

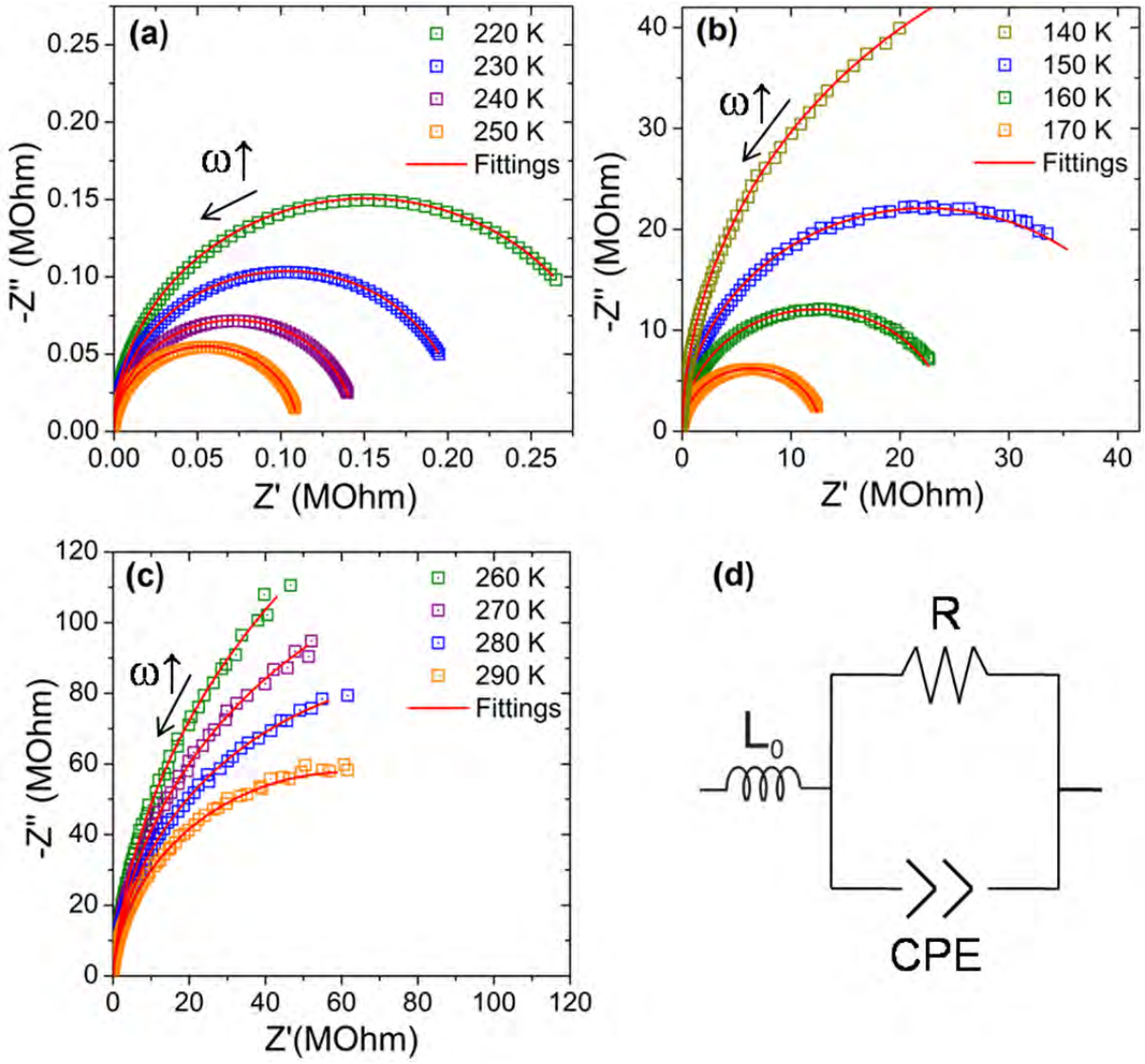

Figure 2. Impedance data recorded at different temperatures of **(a)** $Sr_{0.7}Ba_{0.3}MnO_3$ grown on LSAT; **(b)** $Sr_{0.6}Ba_{0.4}MnO_3$ grown on LSAT; **(c)** $Sr_{0.5}Ba_{0.5}MnO_3$ grown on GSO. **(d)** Equivalent circuit used to fit impedance data. Red solid lines in (a), (b) and (c) denote the fittings of impedance data using Equation (1) –see text– corresponding to the model sketched in (d).

A close inspection of the *–Z'' vs. Z'* impedance complex planes reveals a slight depression of the semicircle. This is at odds with an ideal dielectric response, but commonly observed in most dielectric materials.[17,20,21,23,28] This non-ideality in epitaxial films is ascribed to a certain

distribution of relaxation times (τ = RC) within the sample or inhomogeneities (like oxygen vacancies, for instance).[30,31,32,33] To account for this non-ideality, the capacitance *C* (in the *R*-*C* parallel model) is usually replaced by a constant phase element (CPE),[17,20,21,23,28,30,31,32,33] the impedance of which is given by $Z^*(\mathrm{CPE}) = [Q\cdot(i\omega)^{\alpha}]^{-1}$, where *Q* and *α* ($\alpha \leq 1$, being $\alpha = 1$ the ideal dielectric response) denote the amplitude and the phase of the CPE, respectively.

Thus, taking into account all electrical contributions to the impedance response, impedance data were fitted using the model depicted in Figure 2d, the impedance of which is given by:

$$Z^*_{L_0-R-CPE} = i\omega L_0 + \frac{R}{1+RQ(i\omega)^{\alpha}} \qquad (1)$$

Some fitting results are shown in Figure 2a-c as red solid lines. As observed, the model fits the data reasonably well, and the same holds for the rest of SBMO films and temperatures analyzed in this work. From the fits we can extract L_0, Q, α, and R values at each temperature, T. L_0 is found to display very low values ($L_0 \sim 10^{-6}$ H). The recorded α values were comprised between 0.94 – 1, proving that the deviation of the ideal dielectric response is very small in $Sr_{1-x}Ba_xMnO_3$ thin films compared to other dielectric oxide thin films.[20,21,23] From the fitting values we can compute the capacitance, *C*, using standard procedures.[34] Once $C(T)$ and $R(T)$ are determined, we can assess the temperature dependence of the dielectric and resistive properties of SBMO films.

2.2 Dielectric properties

First we proceed to assess the dielectric response of SBMO films. **Figure 3**a-c show the temperature dependence of the capacitance of SBMO films extracted from the fittings of Equation (1). Note that we have plotted the capacitance values normalized by the capacitance determined at the lowest temperature (≡ C_0 at 10 K), i.e. $C_N(T) \equiv [C(T)-C_0]/C_0$. It is worth remarking that determining the exact quantitative values of the dielectric permittivity of thin films is elusive in the IDE's configuration.[25,26,35] Moreover, the extracted capacitance may also contain substrate contribution, giving unreliable absolute values. Nonetheless, we are interested in relative values

along temperature, pointing to possible polar transition temperature. It is also worth emphasizing that polar materials tend to display large dielectric permittivity values with a non-monotonous temperature dependence, which rises upon increasing temperature showing a maximum around the polar transition temperature.[3,33,36] Thus, assessing $C_N(T)$ of different SBMO films may give some hints on how strain and/or Ba-content may affect their polar nature.

Figure 3d shows the determined $C_N(T)$ of bare LSAT, TSO and GSO substrates treated as if the SBMO films had been grown on top of them (see Supporting information). $C_N(T)$ is fairly constant (less than ~5% of variation) along temperature for all three substrates, as expected for non-polar materials, whose dielectric permittivity yields no remarkable temperature dependence.[37,38,39] Thus, all $C_N(T)$ changes that are observed in Figure 3a-c arise solely from the temperature evolution of the dielectric properties of SBMO films.

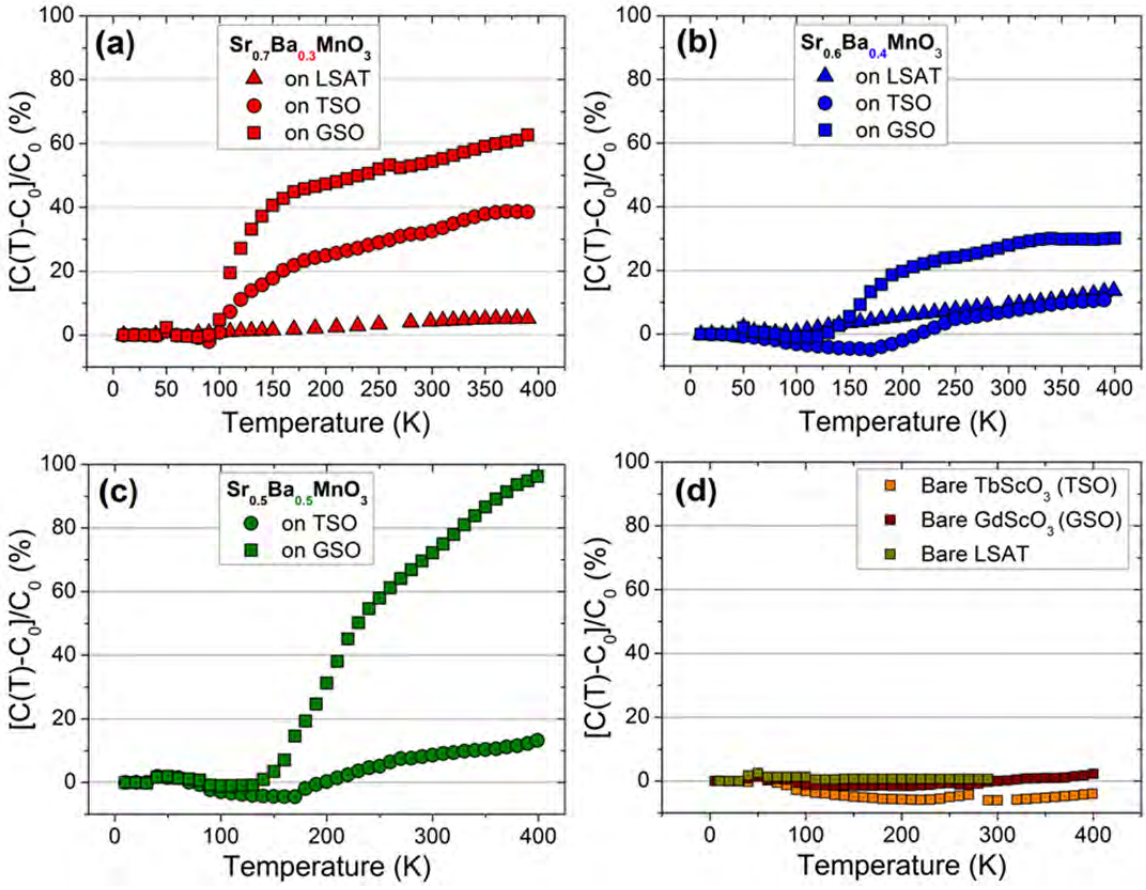

Figure 3. Temperature dependence of the capacitance of **(a)** $Sr_{0.7}Ba_{0.3}MnO_3$, **(b)** $Sr_{0.6}Ba_{0.4}MnO_3$, **(c)** $Sr_{0.5}Ba_{0.5}MnO_3$ thin films and **(d)** bare LSAT, $TbScO_3$ and $GdScO_3$ substrates treated in the same conditions as when the films are grown on top of them. C_0 denote the capacitance at 10 K. Capacitance values are normalized by C_0.

Inspection of $C_N(T)$ of SBMO films (Figure 3a-c) evidences its dependence on the tetragonal distortion of (Sr,Ba)MnO_3 system as depicted in Figure 1a. Focusing first on $Sr_{0.7}Ba_{0.3}MnO_3$ thin films (Figure 3a), we can observe that the maximum $C_N(T)$, occurring between 370 K and 400 K, augments on increasing the tetragonal distortion, i.e. going from ~5% to ~40% and then further to ~60% when the films are grown on LSAT, TSO and GSO, respectively. Thus, $Sr_{0.7}Ba_{0.3}MnO_3$ thin films grown on LSAT, which are nearly cubic, display no remarkable $C_N(T)$ changes, pointing to a non-polar material such as bulk $Sr_{0.7}Ba_{0.3}MnO_3$ specimens which are also cubic. Instead, the significantly larger maximum $C_N(T)$ observed in $Sr_{0.7}Ba_{0.3}MnO_3$ thin films grown on TSO and GSO suggest that polar order might be induced by strain and whose transition temperature is well above room temperature. Similarly, the maximum $C_N(T)$ in $Sr_{0.6}Ba_{0.4}MnO_3$ thin films (Figure 3b) is found around 350 K in those films grown on GSO where the largest tetragonal distortion is achieved, whereas on LSAT and TSO (smaller tetragonal distortions) small $C_N(T)$ values are observed. Note, though, that the largest $C_N(T)$ values achieved in $Sr_{0.6}Ba_{0.4}MnO_3$ thin films (~30% for those grown on GSO) are more modest than those determined in $Sr_{0.7}Ba_{0.3}MnO_3$ thin films grown on TSO and GSO. This correlates with the tetragonal distortion, *t*, which follows: $t(Sr_{0.7}Ba_{0.3}MnO_3/GSO) > t(Sr_{0.7}Ba_{0.3}MnO_3/TSO) > t(Sr_{0.6}Ba_{0.4}MnO_3/GSO)$, as shown in Figure 1a. For $Sr_{0.5}Ba_{0.5}MnO_3$ thin films grown on TSO and GSO (Figure 3c) the maximum $C_N(T)$ is also found in the most tetragonally distorted film, i.e. on GSO. However, this maximum $C_N(T)$ is extremely large (reaching almost 100% at ~400 K) compared to the other SBMO films grown on GSO which possess larger tetragonal distortions. This is possibly due to the fact that Ba-content may have an additional effect, apart from strain, on the polar character in SBMO films, as bulk $Sr_{1-x}Ba_xMnO_3$ specimens are ferroelectric for $x \geq 0.45$ with no strain.[9] **Figure 4** summarizes the dependence of the maximum values of $C_N(T)$ achieved in SBMO films as a function of Ba-content and tetragonal distortion.

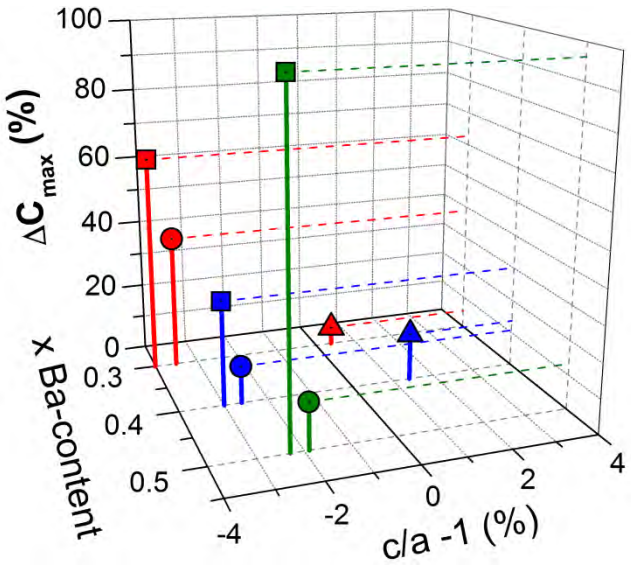

Figure 4. Maximum value of $C_N(T)$ achieved in SBMO films as a function of Ba-content and tetragonal distortion.

In order to further correlate the dielectric properties with the polar order, we have used aberration-corrected scanning transmission electron microscopy (STEM) and the combination of annular bright-field (ABF) and high angle annular dark-field (HAADF) to image the atomic positions of both light (O) and heavy (Sr/Ba and Mn) elements[11,40,41,42] and investigate, at the atomic scale level, ion off-centering displacements [see Experimental section]. For the experiment we have selected two samples grown on TSO: *i*) $Sr_{0.6}Ba_{0.4}MnO_3$ displaying no significant changes of $C_N(T)$ along T and *ii*) $Sr_{0.7}Ba_{0.3}MnO_3$ with remarkable increase of $C_N(T)$ upon increasing T (see Figure 3). As stated previously, under tensile strain the polar axis is expected to lie along <110> directions, hence Mn^{4+} off-centering should occur along these directions. Thus, [110] cross-section TEM specimens were prepared in order to image these ion displacements.

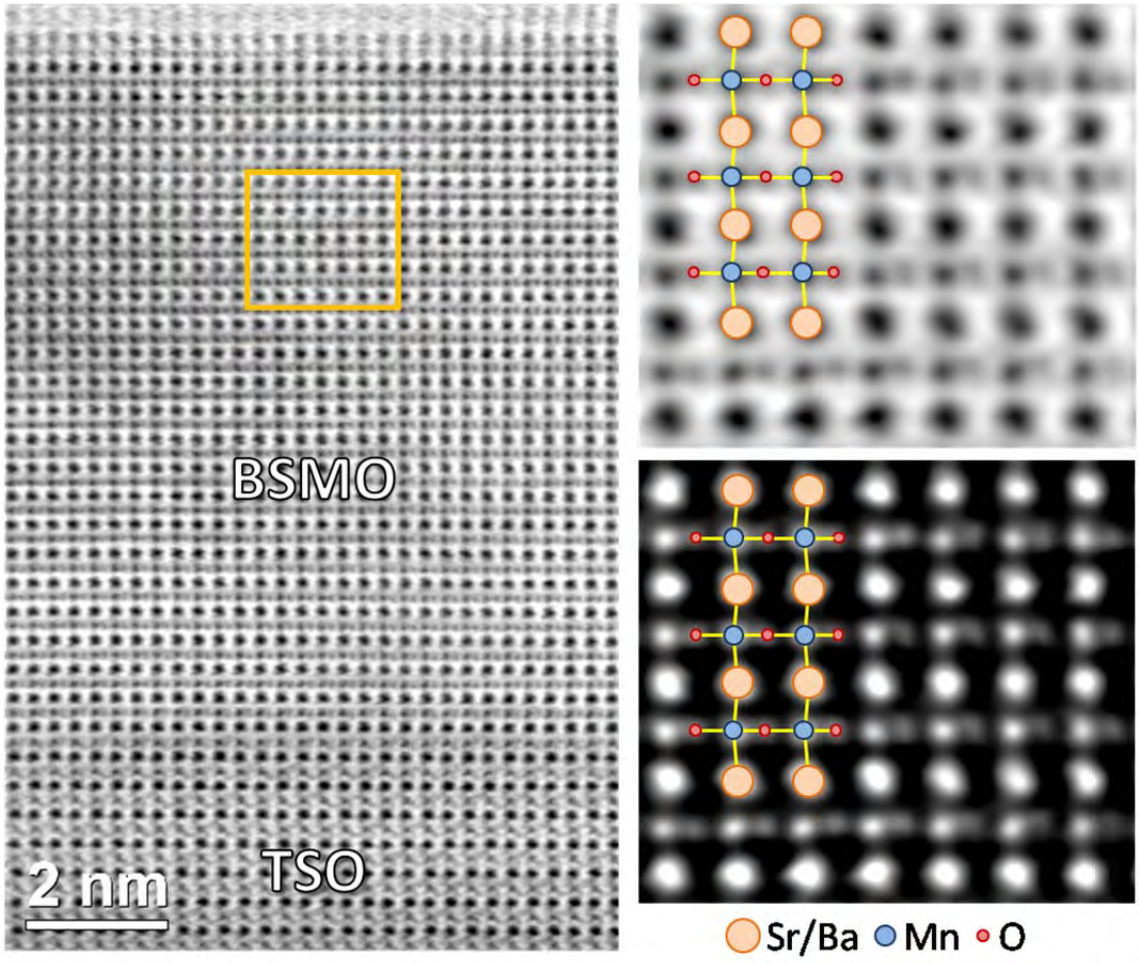

Figure 5. Left panel: ABF images of [110] TEM cross sections of $Sr_{0.7}Ba_{0.3}MnO_3$ film grown on TSO. Right panel: ABF (top) and its inverted-contrast (bottom) magnified images of the area highlighted in the left image, identifying individual atomic columns: Sr/Ba (orange), Mn (blue) and O (red).

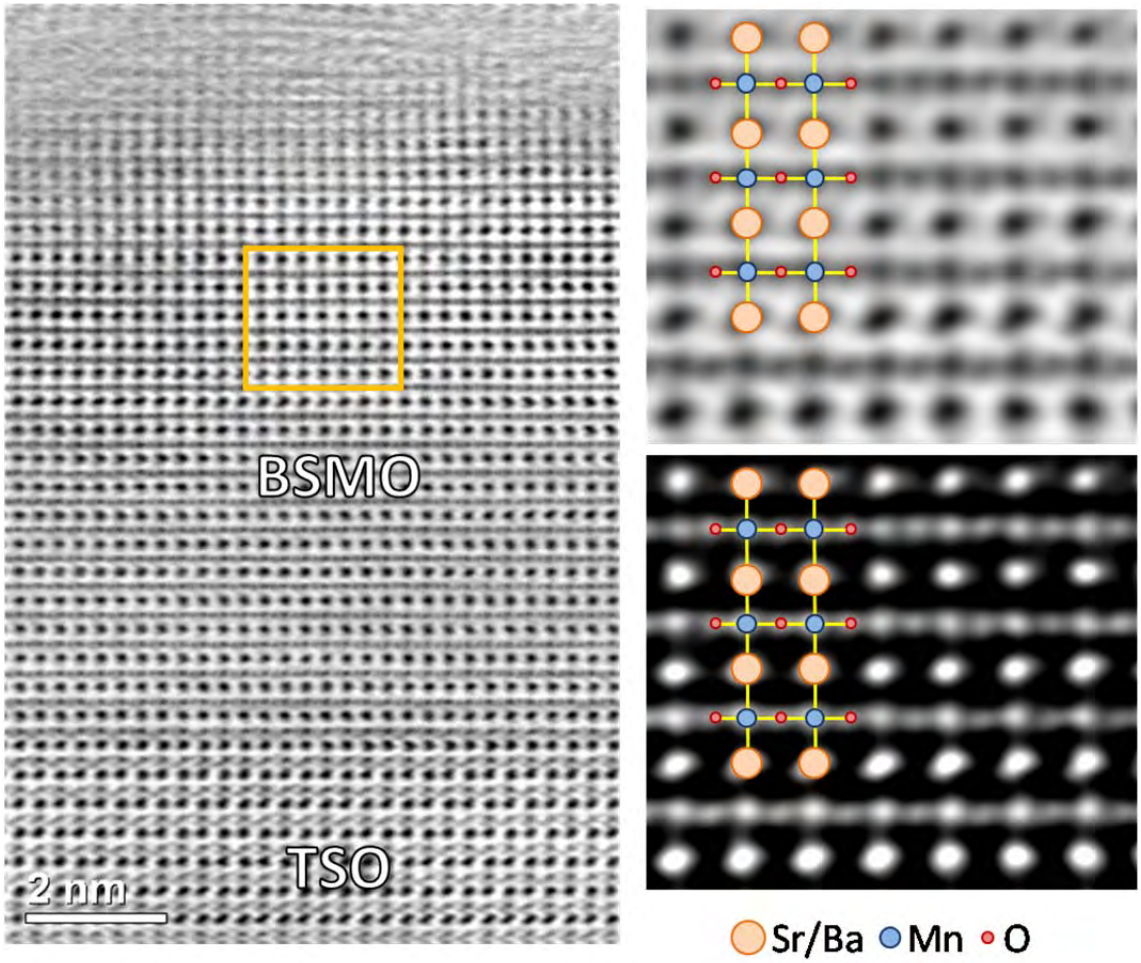

Figure 6. Left panel: ABF images of [110] TEM cross sections of $Sr_{0.6}Ba_{0.4}MnO_3$ film grown on TSO. Right panel: ABF (top) and its inverted-contrast (bottom) magnified images of the area highlighted in the left image, identifying individual atomic columns: Sr/Ba (orange), Mn (blue) and O (red).

Figure 5 shows the ABF and its inverted-contrast image of $Sr_{0.7}Ba_{0.3}MnO_3$ grown on TSO. Individual atomic columns of the perovskite structure are identified, in which some Sr/Ba, Mn, and O columns are artificially colored in orange, blue and red, respectively, for the sake of clarity. As observed, taking the Sr/Ba sublattice as a reference, Mn cations shift from their centrosymmetric position towards the expected in-plane <110> directions. Moreover, a significant O anion off-centering, also along the <110> directions, is clearly revealed, confirming the presence of spontaneous polarization along the in-plane <110> directions. This behavior is also found in polar 20-nm thick SMO thin films grown on LSAT.[11] Thus, results evidence that strained $Sr_{0.7}Ba_{0.3}MnO_3$ thin films grown on TSO, unlike bulk specimens, do display polar order at room temperature, arising from the in-plane tetragonal distortion imposed by the tensile epitaxial strain.

In contrast, for $Sr_{0.6}Ba_{0.4}MnO_3$ grown on TSO (**Figure 6**), in which the in-plane tetragonal distortion is much more modest, just a tiny off-centering of O anions along <110> directions is observed and no evidence of Mn cations displacements is found (they remain in their centrosymmetric position). This leads to a small spontaneous polarization, if it is present at all. These results are in agreement with the temperature evolution of their dielectric properties: the larger the increase of $C_N(T)$ upon temperature, the larger the off-centering displacements of Mn and O ions. Although the off-centering of Mn and O ions were not assessed for all the samples by STEM, it is reasonable to argue that those SBMO films showing a strong increase of the capacitance on increasing temperature, i.e. $Sr_{0.7}Ba_{0.3}MnO_3$, $Sr_{0.6}Ba_{0.4}MnO_3$ and $Sr_{0.5}Ba_{0.5}MnO_3$ on GSO, are likely to be polar as well. Note that this dielectric behavior is a typical feature in ferroelectric materials.[3,33,36]

2.3 Magnetoelectric effect

As shown in **Figure 7**a, for those SBMO films showing large $C_N(T)$, a clear kink in the temperature dependence of the capacitance occurs at a certain temperature, T^*, below which $C_N(T)$ is strongly reduced. T^* depends on the Ba content and substrate, and is comprised between 150 K and 220 K. Interesting enough, in this range of temperatures the onset of the antiferromagnetic order takes place.[6,9,10] In bulk SBMO specimens the Néel temperature, T_N, slightly diminishes upon Ba-content from 230 K (x = 0) to around 200 K (x = 0.5).[9] Yet a more significant reduction of T_N can be obtained by tensile epitaxial strain,[6,10] in which T_N of SMO thin films could drop to 120 K by 2% strain. In our SBMO films T^* decreases on increasing the tetragonal distortion (Figure 7b) corresponding to an increase of tensile strain.

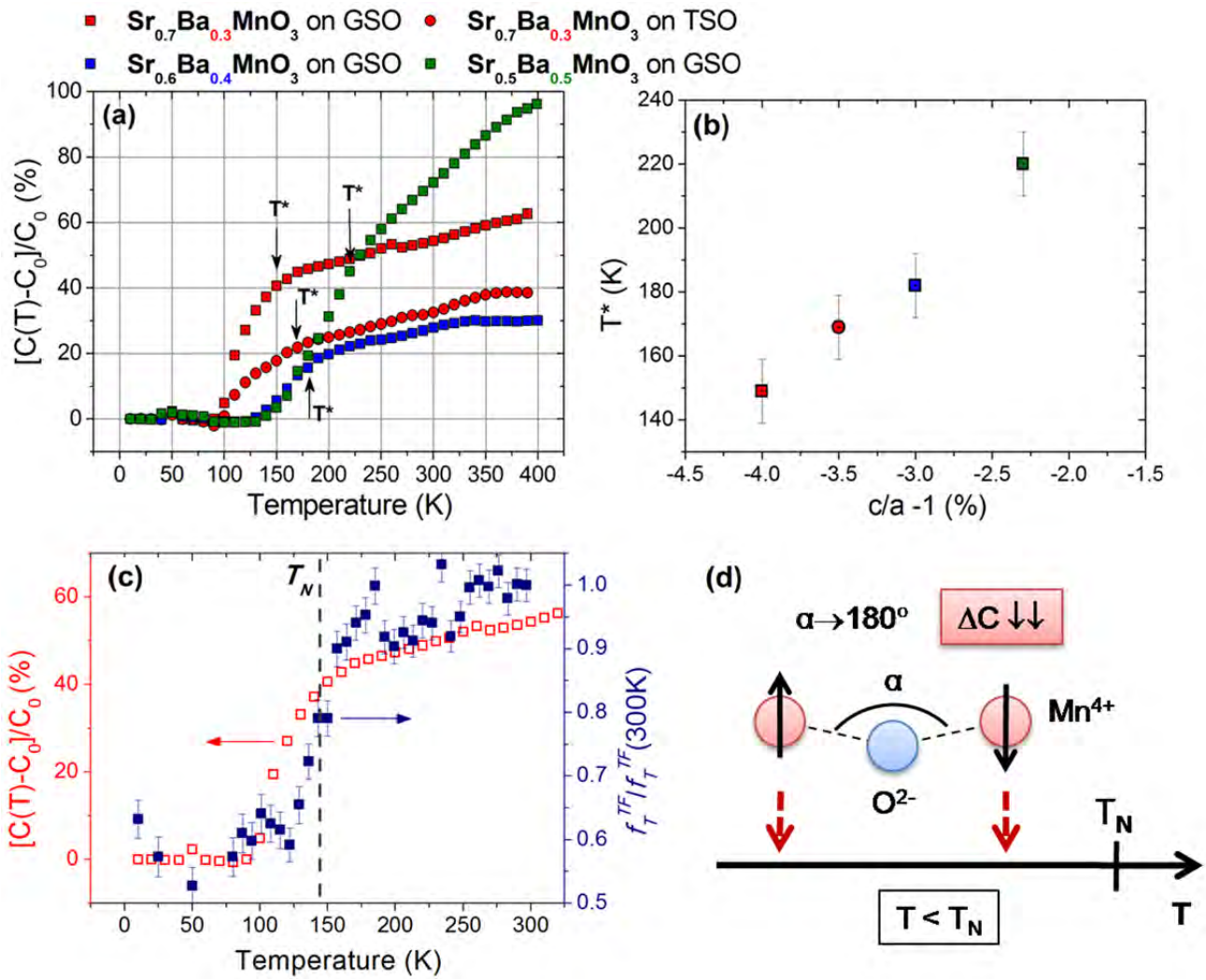

Figure 7. (a) Temperature dependence of the capacitance of $Sr_{0.7}Ba_{0.3}MnO_3$ films on TSO, $Sr_{0.7}Ba_{0.3}MnO_3$ films on GSO, $Sr_{0.6}Ba_{0.4}MnO_3$ films on GSO and $Sr_{0.5}Ba_{0.5}MnO_3$ films on GSO. T* denotes the temperature at which a kink occurs in the temperature dependence of the capacitance. **(b)** Dependence of T* on the tetragonal distortion of $Sr_{1-x}Ba_xMnO_3$ thin films. **(c)** Temperature dependence of the capacitance of $Sr_{0.7}Ba_{0.3}MnO_3$ films on GSO (left axis); temperature dependence of the transverse fraction f_T^{TF} determined in an external transverse magnetic field of 10 mT for E_{impl} = 1 keV, normalized to the fraction at 300 K for $Sr_{0.7}Ba_{0.3}MnO_3$ film on GSO (right axis). The dashed line denotes the Néel temperature, T_N, determined as explained in the text. **(d)** Sketch showing the partial recovering of the centrosymmetric position of Mn^{4+} below T_N.

In order to shed some light on the antiferromagnetic transition temperature, low energy Muon spin relaxation and rotation (LE-μSR) measurements were performed [See Experimental section and Supporting Material].[10,43,44,45] The Néel temperature has been determined from temperature scans in a weak magnetic field B_{ext} applied perpendicular to the initial muon spin polarization and to the film surface. The method used here to determine the Néel temperature is identical to the one described in Ref. [10]. The decay rate of the muon spin polarization is described by the relaxation function:

$$G_x(t) = f_T^{TF} \cos(\gamma_\mu B_{ext} t + \phi) e^{-\lambda_T t} + f_L^{TF} e^{-\lambda_L t} \quad (2)$$

f_T^{TF} and f_L^{TF} reflect the fraction of the muons having their spin initially transverse and longitudinal to the local magnetic field direction, respectively; γ_μ is the gyromagnetic ratio of the muon, λ_T the relaxation rate and ϕ is a phase offset [See Supporting material]. The fitting of the relaxation function $G_x(t)$ was performed using the musrfit program.[46]

Above T_N (in the paramagnetic regime), f_T^{TF} is at its maximum since only B_{ext} is present inside the sample. Below T_N, the superposition of the small external B_{ext} and the internal magnetic fields in the sample leads to a strong dephasing of the precession signal. This produces a decrease of f_T^{TF} to a level corresponding to the nonmagnetic volume fraction of the sample. Figure 7c (right) illustratively shows the transverse fraction, f_T^{TF}, as a function of temperature for a $Ba_{0.3}Sr_{0.7}MnO_3$ film grown on GSO. This compound has been selected as a representative of this study due to the sharp drop occurring in the capacitance around T*. The data are normalized to the values in the paramagnetic regime at 300 K. The magnetic transition manifests as a decay of the transverse fraction, f_T^{TF}/ f_T^{TF}(300 K), at a temperature around 150 K. T_N is obtained by fitting the derivative curve of the data with a Gaussian curve and taking its center as T_N.[10] This yields a value of $T_N \approx$ 144 K, which coincides with the strong reduction of the capacitance (Figure 7c, left).

Thus, we identify $T^* = T_N$ and, consequently, we deduce that the drop in the capacitance values of SBMO films arises from the emergence of the antiferromagnetic order. It is interesting to note that in $EuTiO_3$ the dielectric constant decreases as well, when ordered antiferromagnetically, yet displaying a much more modest reduction (~3.5%) around T_N.[47] An order of magnitude larger reduction (~32%) is found in bulk SMO.[48] In epitaxial SBMO films this antiferromagnetism-induced reduction can reach even larger values (Figure 7a), displaying an extremely large magnetoelectric effect compared to other magnetoelectric oxides. More important, this coupling between magnetism and dielectric properties can be tuned from ~18% to ~50% by appropriately selecting both Ba-content and epitaxial strain (Figure 7a).

The origin of this magnetoelectric coupling can be argued in terms of the strong spin-phonon coupling of these compounds.[6,7,48,49,50] In both $EuTiO_3$ and (Sr,Ba)MnO_3 compounds it is the soft phonon mode (the Ti and Mn, respectively, moving in the opposite direction of the surrounding oxygens in the octahedron), which mainly contributes to the dielectric constant.[47,48,50] The soft mode significantly stiffens when the antiferromagnetic order emerges,[47,48,50] yielding a decrease in the dielectric permittivity following $\varepsilon(T) = \varepsilon_{PM}(1 + \alpha\langle \boldsymbol{S}_i \cdot \boldsymbol{S}_j \rangle)$, where ε_{PM} is the dielectric permittivity in the paramagnetic regime, $\langle \boldsymbol{S}_i \cdot \boldsymbol{S}_j \rangle$ is the nearest-neighbour spin correlation function, and α is the coupling constant between spin correlation and dielectric permittivity.[47] In the antiferromagnetic regime $\alpha\langle \boldsymbol{S}_i \cdot \boldsymbol{S}_j \rangle < 0$ [Ref. 47, 50]. In $EuTiO_3$, the spin order of Eu cations on the A-site of the perovskite couples indirectly with the Ti – O soft mode, whereas in (Sr,Ba)MnO_3 the Mn magnetic cations are placed on the B-site, directly affecting the Mn – O soft mode. In particular, the antiferromagnetic superexchange interaction promotes the alignment of Mn – O – Mn bond (as shown Figure 7d).[12] Thus, Mn partially recovers its centrosymmetric position in the antiferromagnetic regime, entailing a reduction of the electric dipole moment. This has been experimentally observed as a reduction of the tetragonality in bulk $Sr_{0.5}Ba_{0.5}MnO_3$ (Ref. [9]) and a reduction of the noncentrosymmetric distortion in epitaxial $SrMnO_3$ thin films below T_N.[8] It is interesting to note that the films displaying the largest increase of $C_N(T)$ upon temperature and, thus, the largest off-centering displacements of Mn and O ions show the greatest reduction of the capacitance values when the antiferromagnetic order emerges. This possibly comes from the fact that the larger the off-centering displacements are above T_N, the more pronounced the change is when the antiferromagnetic order promotes the partially centrosymmetric recovering.

The direct coupling between the Mn spins with the Mn – O soft mode together with the much stronger antiferromagnetic superexchange interaction in (Sr,Ba)MnO_3 compared to $EuTiO_3$ (showing T_N = 5.5. K)[47] may explain the much larger coupling between magnetism and dielectric properties in (Sr,Ba)MnO_3 compounds. On the other hand, the soft mode in (Sr,Ba)MnO_3 system softens by increasing Ba content[50] and the magnitude of spin-phonon coupling can be modified by

epitaxial strain,[6] which enables the possibility to control the magnetoelectric coupling in (Sr,Ba)MnO_3 system by both strain engineering and chemical pressure as shown in Figure 7a.

2.4 Semiconducting properties

Now we go on to assess the resistive properties of SBMO films extracted from fittings using Equation (1). The temperature dependence of the resistance of $Sr_{0.7}Ba_{0.3}MnO_3$ films grown on LSAT, TSO and GSO shows a semiconductor-like behavior, in which the resistance decreases upon temperature (**Figure 8**a). The same trend is found for the rest of SBMO thin films analyzed in this work (results not shown). At intermediate and high temperatures a linear dependence between the resistance, *R*, in log scale and the reciprocal temperature (1/T) is found (Figure 8b), following an Arrhenius law, which is extended to the rest of SBMO films. Thus, considering the simplest picture of a semiconductor conduction mechanism with band gap energy E_g, the values of *R* at high and intermediate temperatures were fitted following: $R(T) = R_0 \exp[E_g/(2k_B \cdot T)]$, where R_0 is a pre-exponential factor and k_B is the Boltzmann constant. The fits are indicated by the solid blue lines in Figure 8b for the $Sr_{0.7}Ba_{0.3}MnO_3$ films. The determined E_g values for the SBMO films analyzed in this work are shown in Figure 8c, plotted as a function of the unit cell volume.[14] As observed, there is a clear trend of increasing E_g with the expanding the unit cell of SBMO thin films, going from ~0.25 eV to ~0.48 eV. The obtained E_g values confirm the expected small band gap in these compounds.[6,24] Interesting enough, they are in good agreement with the predicted evolution of E_g with strain in SMO thin films: between 0.22 eV (for 0% strained film) and 0.51 eV (for 5% tensile-strained film).[6] It is worth noting that the unit cell volume of SBMO thin films not only increases on increasing the Ba-content but also on increasing tensile strain.[14] Hence, by simultaneously using Ba-content and strain we may gain a huge versatility to control the band gap energy, and thus the semiconducting properties, of (Sr,Ba)MnO_3 system.

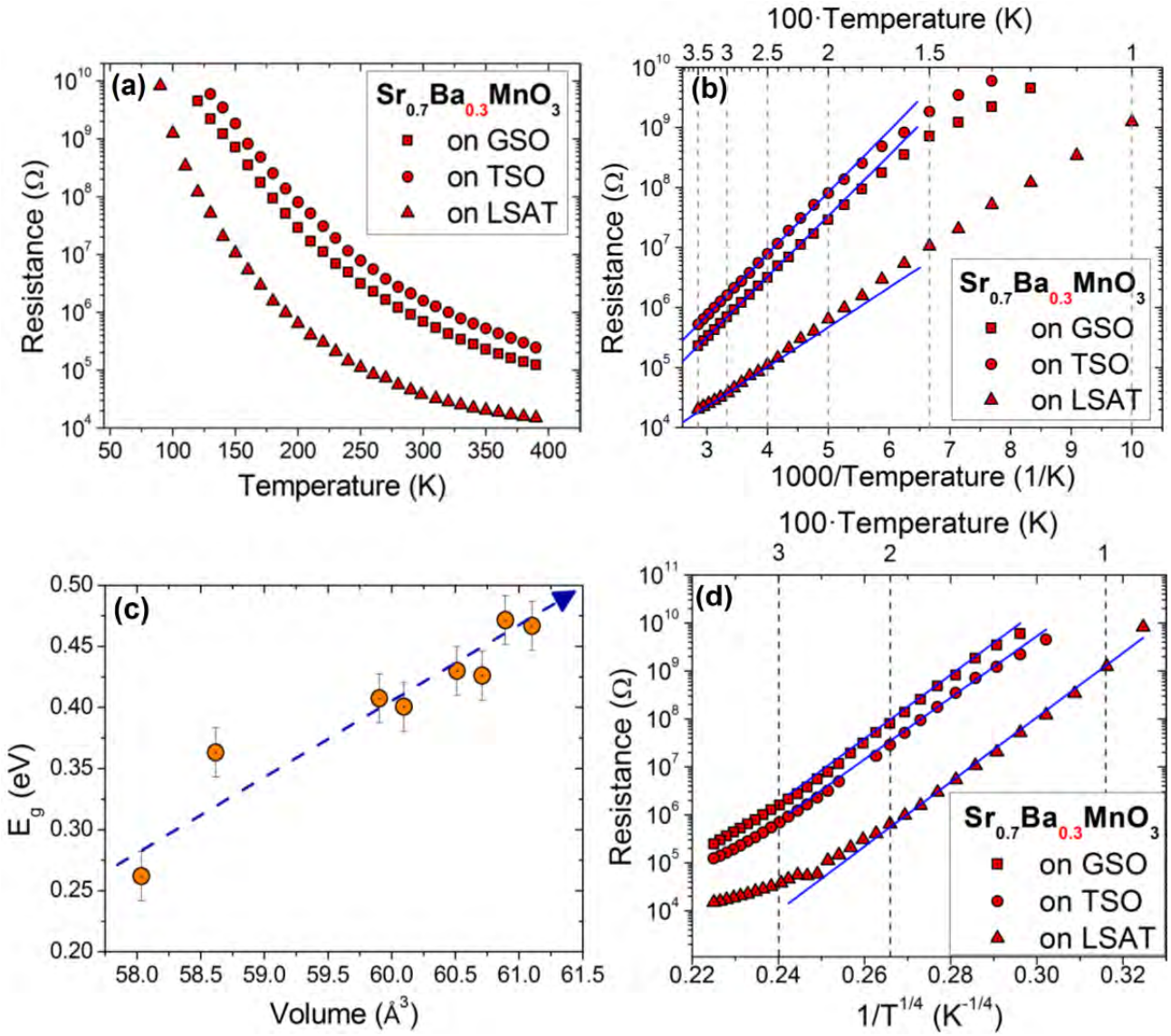

Figure 8. (a) Temperature dependence of the resistance and **(b)** Resistance plotted as a function of the reciprocal of temperature of $Sr_{0.7}Ba_{0.3}MnO_3$ thin films grown on LSAT, TSO and GSO. Blue solid lines indicate the fits to the Arrhenius law at high and intermediate temperatures. **(c)** Energy band gap of SBMO thin films as a function of the unit cell volume. Dashed blue arrow serves as guide-to-eye. **(d)** Resistance *vs.* $1/T^{1/4}$ of $Sr_{0.7}Ba_{0.3}MnO_3$ thin films grown on LSAT, TSO and GSO. Blue solid lines indicate the fits to variable-range-hopping conduction mechanism at low temperatures.

At low temperatures $R(T)$ deviates from the Arrhenius law (Figure 8b), indicating a change in the transport mechanism or a different activation energy. A similar behavior was previously observed in $SrMnO_3$ films deposited on $SrTiO_3$,[51] in which a transition from a thermal-activated band conduction mechanism to variable range hopping (VRH) between localized states occurs at 205 K. This phenomenon is widely found in many other semiconductor materials, in which at sufficiently low temperatures the thermal energy is too low for band conduction dominating mechanism.[52,53,54,55,56] VRH mechanisms follows $R(T) = R_0\exp[(T_0/T)^{\alpha}]$, where T_0 is a constant and

α = 1/4 for three-dimensional hopping.[51,53,54,55,56] This model was used to fit the temperature dependence of the resistance in our films below 180 K. Figure 8d illustratively shows the results of $Sr_{0.7}Ba_{0.3}MnO_3$ films. The obtained T_0 fit values, ≈ 5×10^8 K – 6×10^8 K, are in the same order of magnitude as the ones obtained previously in SMO thin films.[51] The good agreement between the experimental data and the model implies that VRH might be the mechanism that dominates the conduction in our films at low temperature.

3. Conclusions

For the first time the electrical and magnetoelectric properties of epitaxial strained $Sr_{1-x}Ba_xMnO_3$ thin films in the perovskite phase have thoroughly been investigated. We prove that these properties are severely altered by lattice distortions caused either by Ba-content or epitaxial strain. We demonstrate that polar order at room temperature can be induced in $Sr_{1-x}Ba_xMnO_3$ thin films when the tensile epitaxial strain is large enough, even for x = 0.3 and x = 0.4, thus overcoming bulk-specimens-limitation, which become polar only above x = 0.45 Ba-doping. Polar order correlates with the temperature dependence of the dielectric properties, which show a strong increase of the capacitance values on increasing temperature, a common feature of ferroelectric materials. On the other hand, the dielectric properties strongly couple with the magnetic properties, yielding a steep drop of the capacitance values when Mn magnetic moments order antiferromagnetically. More important, this strong reduction of the capacitance below the Néel temperature can be tuned from ~18% to ~50% by appropriately selecting both Ba-content and epitaxial strain, providinga huge control over the magnetoelectric response in $Sr_{1-x}Ba_xMnO_3$ films. Finally, we demonstrate that $Sr_{1-x}Ba_xMnO_3$ thin films show a semiconductor-like behavior, with a thermally-activated conduction band mechanism for intermediate and high temperatures, whereas variable-range hopping mechanism prevails at low temperatures. The band gap energy, E_g, of $Sr_{1-x}Ba_xMnO_3$ thin films is in the range 0.2 – 0.5 eV, in agreement with previous theoretical predictions for $SrMnO_3$. Yet a clear trend of increasing E_g on increasing the unit cell volume of $Sr_{1-x}Ba_xMnO_3$

thin films either by strain or Ba-content is found, offering the possibility of band gap engineering in (Sr,Ba)MnO_3 system. Thus, our findings lay the foundation for designing at will the electrical properties, such as dielectric and semiconducting, and the magnetoelectric coupling in $Sr_{1-x}Ba_xMnO_3$ films by simultaneously using strain engineering and chemical pressure.

4. Experimental Section

Thin film growth. $Sr_{1-x}Ba_xMnO_3$, $0.3 \leq x \leq 0.5$, thin films were grown by pulsed laser deposition (PLD) onto $(LaAlO_3)_{0.3}$-$(Sr_2AlTaO_6)_{0.7}$ (LSAT), $TbScO_3$ (TSO) and $GdScO_3$ (GSO), having an average pseudocubic lattice parameter of ≈ 3.87 Å, ≈ 3.96 Å and ≈ 3.97 Å, respectively. All the substrates used are (001)-oriented, assuming a pseudocubic lattice. Note that $TbScO_3$ and $GdScO_3$ are actually orthorhombic and (110)-oriented. Still, with this orientation the orthorhombic structure can be described as a distorted pseudocubic structure, in which the new pseudocubic in-plane lattice parametes are obtained computing $a_{pc} = (1/2)(a_o^2 + b_o^2)^{1/2}$ and $b_{pc} = (1/2)(c_o)$, where "pc" and "o" subscripts denote pseudocubic and orthorhombic, respectively. For the sake of simplicity in this work we have used the pseudocubic notation with an average pseudocubic lattice parameter. Note that despite $a_{pc} \neq b_{pc}$, their values are very similar, see, for instance, Ref. [57]. Laser fluence and repetition rate were set at ≈ 1 J/cm^2 and 10 Hz, respectively. Substrate temperatures and oxygen pressure during the growth process were fixed at 1000 °C and $5x10^{-5}$ Torr, respectively. After deposition the films were cooled down at 10 °C/min in a pure oxygen atmosphere (700 Torr). The structural characterization of the films was carried out by X-ray diffraction (XRD) with a Bruker D8 Advance high-resolution diffractometer. The sample growth, perovskite phase stability and structure of $Sr_{1-x}Ba_xMnO_3$ films are reported elsewhere.[14]

Interdigital electrodes (IDE's). IDE's were prepared by means of optical lithography and metal sputtering. Several steps take place in the lithography process: *i*) the negative resin TI35ES is spinned on top of the film; *ii*) after warming, ultraviolet (UV) light goes through a photomask with the IDE's patron aligned on the film + resin, chemically altering the UV exposed region of the resin; *iii*) After warming, the whole sample (film + resin) is again exposed to UV light; *iv*) sample

(film + resin) is immersed in developer, dissolving the region of the resin that have been exposed twice under UV light, imprinting the IDE's patron onto the resin. Cr/Al bilayer was afterwards deposited onto resin + film with the imprinted-IDE's-patron by sputtering. By lift-off process the resin is removed and only the Cr/Al bilayer following the IDE's patron remains on the film. The so-formed IDE's electrodes consist of 114 interdigital electrodes, with 8 μm finger spacing. Optical lithography was carried out in 100-class clean room facility. The following electrical measurements were performed using IDE's.

Electrical characterization. Impedance spectroscopy was performed using Agilent 4294A Precision Impedance Analyser, operating from 40 Hz to 110 MHz. Due to the increase of the inductance component upon frequency of the experimental set up, experiments were performed up to 20 MHz. The amplitude of the applied excitation voltage was set to V_{ac} = 250 mV. Impedance spectroscopy measurements were carried out at zero magnetic field. Complex impedance data of $Sr_{1-x}Ba_xMnO_3$ thin films were collected in terms of modulus, $|Z|$, and phase, θ, and converted to real part, $Z' = |Z|\cos\theta$, and imaginary part, $Z'' = |Z|\sin\theta$. Fitting impedance data using model Equation (1) was carried out by commercial software *Zview*®. Samples were placed in a home-made coaxial electrical probe holder, introduced into a helium-flux-controlled-operating cryostat that works from 10 K to 400 K.

Scanning transmission electron microscopy (STEM) characterization. (110) Cross-sectional specimens of $Sr_{0.7}Ba_{0.3}MnO_3$ and $Sr_{0.6}Ba_{0.4}MnO_3$ films grown on TSO were prepared by conventional mechanical polishing and low-voltage Ar+ ion milling for the final thinning. Aberration-corrected STEM analyses were carried out in a probe-corrected FEI Titan 60–300 microscope operated at 300 kV, fitted with a high-brightness field-emission gun (X-FEG) and a CEOS probe Cs corrector, obtaining a probe size below 1 Å. Atomic-resolution images were obtained by combining HAADF and ABF imaging in STEM, with a convergence angle of 25 mrad. The inner and outer collection angles of the HAADF detector were 48 and 200 mrad, respectively;

for the ABF detector were 8 and 22 mrad, respectively. The obtained raw images were filtered to reduce background noise.

Magnetic characterization. Muon spin relaxation and rotation (μSR) measurements were carried out using the low-energy muon spectrometer (LEM) at the μE4 beamline at the Paul Scherrer Institut (PSI, Switzerland).[43] In μSR experiments spin-polarized positive muons are implanted into a sample and thermalized [See Supporting Information]. By tuning the implantation energy between 1 and 30 keV, mean depths between 10 nm and few hundred nanometers can be chosen. To determine where the muons would implant within the sample we carried out Monte Carlo simulations using the TRIM.SP.[58] Results for these calculations for different implantation energies for the 15.5 nm thick $Ba_{0.3}Sr_{0.7}MnO_3$ film deposited on a $GdScO_3$ substrate are shown in Figure S7 of Supporting Information. By tuning the energy between 1 and 5 keV the mean stopping depth of the muons can be varied in a range of 6 – 30 nm in this film. The data presented here were obtained with a muon implantation energy E_{imp}= 1 keV. This energy yields a mean implantation depth of about 6 nm and approximately 80 % of the muons stopped at the $Ba_{0.3}Sr_{0.7}MnO_3$ film. The sample was glued with silver paint on a nickel coated aluminum plate. The experiments were performed in ultrahigh vacuum at a pressure of 10^{-9} mbar in the temperature range 5 – 300 K. LE-μSR measurements were carried out in a weak transverse magnetic field of 10 mT to obtain the magnetic transition temperature T_N.

Supporting Information

Supporting Information is available from the Wiley Online Library or from the author.

Acknowledgements

Financial support from Spanish Ministerio de Economía y Competitividad through project MAT2014-51982-C2 and from regional Gobierno de Aragón through project E26 including FEDER funding is also acknowledged. The low-energy μSR measurements have been performed at the Swiss Muon Source SμS, Paul Scherrer Institut, Villigen, Switzerland. R.G. and C.M. were funded by the European Union under the Seventh Framework Programme under a contract for an Integrated Infrastructure Initiative Reference 312483-ESTEEM2. R.G. was also supported by the ERC StG "STEMOX" 239739.

References

[1] J. M. Rondinelli, N. A. Spaldin, *Adv. Mater*. **2011**, *23*, 3363.

[2] E. Dagotto, Y. Tokura, *MRS Bull.* **2008**, *33*, 1037.

[3] N. Izyumskaya, Ya. Alivov, H. Morkoç, *Crit. Rev. Solid State Mater. Sci*. **2009**, *34*, 89.

[4] D. G. Schlom, L.–Q. Chen, C. J. Fennie, V. Gopalan, D. A. Muller, X. Pan, R. Ramesh, R. Uecker, *MRS Bull.* **2014**, *39*, 118.

[5] J. M. Rondinelli, A. S. Eidelson, N. A. Spaldin, *Phys. Rev. B* **2009**, *79*, 205119.

[6] J. H. Lee, K. M. Rabe, *Phys. Rev. Lett.* **2010**, *104*, 207204.

[7] J. Hong, A. Stroppa, J. Íñiguez, S. Picozzi, D. Vanderbilt, *Phys. Rev. B* **2012**, *85*, 54417.

[8] C. Becher, L. Maurel, U. Aschauer, M. Lilienblum, C. Magén, D. Meier, E. Langenberg, M. Trassin, J. Blasco, I. P. Krug, P. A. Algarabel, N. A. Spaldin, J. Pardo, M. Fiebig, *Nat. Nanotechnol.* **2015**, *10*, 661.

[9] H. Sakai, J. Fujioka, T. Fukuda, D. Okuyama, D. Hashizume, F. Kagawa, H. Nakao, Y. Murakami, T. Arima, A. Q. R. Baron, Y. Taguchi, Y. Tokura, *Phys. Rev. Lett.* **2011**, *107*, 137601.

[10] L. Maurel, N. Marcano, T. Prokscha, E. Langenberg, J. Blasco, R. Guzmán, A. Suter, C. Magén, L. Morellón, M. R. Ibarra, J. A. Pardo, P. A. Algarabel, *Phys. Rev. B* **2015**, *92*, 024419.

[11] R. Guzmán, L. Maurel, E. Langenberg, A. R. Lupini, P. A. Algarabel, J. A. Pardo, C. Magén, *Nano Letters* **2016**, *16*, 2221.

[12] G. Giovannetti, S. Kumar, C. Ortix, M. Capone, J. van den Brink, *Phys. Rev. Lett.* **2012**, *109*, 107601.

[13] M. D. Glinchuk, E. A. Eliseev, Y. Gu, L. –Q. Chen, V. Gopalan, A. N. Morozovska, *Phys. Rev. B* **2014**, *89*, 014112.

[14] E. Langenberg, R. Guzmán, L. Maurel, L. Martínez de Baños, L. Morellón, M. R. Ibarra, J. Herrero-Martín, J. Blasco, C. Magén, P. A. Algarabel, J. A. Pardo, *ACS Appl. Mater. Interfaces* **2015**, *7*, 23967.

[15] B. Dabrowski, O. Chmaissem, J. Mais, S. Kolesnik, J. D. Jorgensen, S. Short, *J. Solid State Chem.* **2003**, *170*, 154.

[16] T. Negas, *J. Solid State Chem.* **1973**, *6*, 136.

[17] J. R. Macdonald, *Impedance Spectroscopy*, Wiley, New York, USA **1987**.

[18] J. T. S. Irvine, D. C. Sinclair, A. R. West, *Adv. Mater.* **1990**, *2*, 132.

[19] N. Ortega, A. Kumar, P. Bhattacharya, S. B. Majumder, R. S. Katiyar, *Phys. Rev. B* **2008**, *77*, 014111.

[20] R. Schmidt, J. Ventura, E. Langenberg, N. M. Nemes, C. Munuera, M. Varela, M. García-Hernández, C. León, J. Santamaría, *Phys. Rev. B* **2012**, *86*, 035113.

[21] E. Langenberg, I. Fina, J. Ventura, B. Noheda, M. Varela, J. Fontcuberta, *Phys. Rev. B* **2012**, *86*, 085108.

[22] M. Li, M. J. Pietrwski, R. A. de Souza, H. Zhang, I. M. Reaney, S. N. Cook, J. A. Kilner, D. C. Sinclair, *Nat. Mater.* **2014**, *13*, 31.

[23] W. Bai, C. Chen, J. Yang, Y. Zhang, R. Qi, R. Huang, X. Tang, C.–G. Duan, J. Chu, *Sci. Rep.* **2015**, *5*, 17846.

[24] R. Søndenå, P. Ravindran, S. Stolen, T. Grande, M. Hanfland, *Phys. Rev. B* **2006**, *74*, 144102.

[25] N. J. Kidner, A. Meier, Z. J. Homrighaus, B. W. Wessels, T. O. Mason, E. J. Garboczi, *Thin Solid Films* **2007**, *515*, 4588.

[26] J.–G. Ramirez, R. Schmidt, A. Sharoni, M. E. Gómez, I. K. Schuller, E. J. Patiño, *Appl. Phys. Lett.* **2013**, *102*, 063110.

[27] O. Diéguez, K. M. Rabe, D. Vanderbilt, *Phys. Rev. B* **2005**, *72*, 144101.

[28] P. Lunkenheimer, V. Bobnar, A. V. Pronin, A. I. Ritus, A. A. Volkov, A. Loidl, *Phys. Rev. B* **2002**, *66*, 052105.

[29] G. Catalan, *Appl. Phys. Lett.* **2006**, *88*, 102902.

[30] F. D. Morrison, D. J. Jung, J. F. Scott, *J. Appl. Phys.* **2007**, *101*, 094112.

[31] R. Schmidt, A. W. Brinkman, *J. Appl. Phys.* **2008**, *103*, 113710.

[32] R. Schmidt, W. Eerenstein, T. Winiecki, F. D. Morrison, P. A. Midgley, *Phys. Rev. B* **2007**, *75*, 245111.

[33] A. R. West, D. C. Sinclar, N. Hirose, *J. Electroceramics* **1997**, *1*, 65.

[34] C. H. Hsu, F. Mansfeld, *Corrosion* **2001**, *57*, 747.

[35] O. G. Vendik, S. P. Zubko, M. A. Nikolskii, *Tech. Phys.* **1999**, *44*, 349.

[36] A. F. Devonshire, *Advances in Physics* **1954**, *3*, 85.

[37] S. Coh, T. Heeg, J. H. Haeni, M. D. Biegalski, J. Lettieri, L. F. Edge, K. E. O'Brien, M. Bernhagen, P. Reiche, R. Uecker, S. Trolier-McKinstry, D. G. Schlom, D. Vanderbilt, *Phys. Rev. B* **2010**, *82*, 064101.

[38] T. Kiwa, M. Tonouchi, *Jpn. J. Appl. Phys.* **2001**, *40*, L38.

[39] V. Bovtun, V. Pashkov, D. Nuzhnyy, M. Kempa, V. Goian, V. Molchanov, Y. Poplavko, Y. Yakymenko, S. Kamba, *Microwave and Telecommunication Technology (CriMiCo), 23rd International Crimean Conference*, **2013**, 643.

[40] S. D. Findlay, N. Shibata, H. Sawada, E. Okunishi, Y. Kondo, Y. Ikuhara, *Ultramicroscopy* **2010**, *110*, 903.

[41] S. D. Findlay, N. Shibata, H. Sawada, E. Okunishi, Y. Kondo, T. Yamamoto, Y. Ikuhara, *Appl. Phys. Lett.* **2009**, *95*, 191913.

[42] M. Haruta, H. Kurata, *Sci. Rep.* **2012**, *2*, 252.

[43] T. Prokscha, E. Morenzoni, K. Deiters, F. Foroughi, D. George, R. Kobler, A. Suter, V. Vrankovic, *Nucl. Instrum. Methods Phys. Res., Sect. A* **2008**, *595*, 317.

[44] A. Yaouanc, P. Dalmas de Réotier, *Muon Spin Rotation, Relaxation, and Resonance-Applications to Condensed Matter*, Oxford University Press, Oxford, UK **2011**.

[45] E. Morenzoni, T. Prokscha, A. Suter, H. Luetkens, R. Khasanov, *J. Phys.: Condens. Matter* **2004**, *16*, S4583.

[46] A. Suter, B. M. Wojek, *Phys. Procedia* **2012**, *30*, 69.

[47] T. Katsufuji, H. Takagi, *Phys. Rev. B* **2001**, *64*, 054415.

[48] S. Kamba, V. Goian, V. Skoromets, J. Hejtmánek, V. Bovtun, M. Kempa, F. Borodavka, P. Vanek, A. A. Belik, J. H. Lee, O. Pacherová, K. M. Rabe, *Phys. Rev. B* **2014**, *89*, 064308.

[49] C. J. Fennie, K. M. Rabe, *Phys. Rev. Lett.* **2006**, *97*, 267602.

[50] H. Sakai, J. Fujioka, T. Fukuda, M. S. Bahramy, D. Okuyama, R. Arita, T. Arima, A. Q. R. Baron, Y. Taguchi, Y. Tokura, *Phys. Rev. B* **2012**, *86*, 104407.

[51] S. J. May, T. S. Santos, A. Bhattacharya, *Phys. Rev. B* **2009**, *79*, 115127.

[52] B. I. Shklivskii, A. L. Efros, *Electronic properties of Doped Semiconductor*, Springer-Verlag, Berlin, Germany **1984**.

[53] J. Fontcuberta, B. Martínez, A. Seffar, S. Piñol, J. L. García-Muñoz, X. Obradors, *Phys. Rev. Lett.* **1997**, *7*, 1122.

[54] A. Seeger, P. Lunkenheimer, J. Hemberger, A. A. Mukhin, V. Y. Ivanov, A. M. Balbashov, A. Loidl, *J. Phys.: Condens. Matter* **1999**, *11*, 3273.

[55] D. Yu, C. Wang, B. L. Wehrenberg, P. Guyot-Sionnest, *Phys. Rev. Lett.* **2004**, *92*, 216802.

[56] L. Zhang, Z.–J. Tang, *Phys. Rev. B* **2004**, *70*, 174306.

[57] R. Uecker, B. Velickov, D. Klimm, R. Bertram, M. Bernhagen, M. Rabe, M. Albrecht, R. Fornari, D. G. Schlom, *J. Cryst. Growth* **2008**, *310*, 2649.

[58] W. Eckstein, *Computer Simulation of Ion-Solid Interactions*, Springer, Berlin, Germany **1991**.